

Thermal and non-thermal emission in the Cygnus X region

W. F. Xu^{1,2}, X. Y. Gao², J. L. Han², and F. S. Liu¹

¹ College of Physical Science and Technology, Shenyang Normal University, Shenyang 110034, PR China

² National Astronomical Observatories, Chinese Academy of Sciences, Jia-20 Datun Road, Chaoyang District, Beijing 100012, PR China

Received; accepted

ABSTRACT

Context. Radio continuum observations detect non-thermal synchrotron and thermal bremsstrahlung radiation. Separation of the two different emission components is crucial to study the properties of diffuse interstellar medium. The Cygnus X region is one of the most complex areas in the radio sky which contains a number of massive stars and H II regions on the diffuse thermal and non-thermal background. More supernova remnants are expected to be discovered.

Aims. We aim to develop a method which can properly separate the non-thermal and thermal radio continuum emission and apply it to the Cygnus X region. The result can be used to study the properties of different emission components and search for new supernova remnants in the complex.

Methods. Multi-frequency radio continuum data from large-scale surveys are used to develop a new component separation method. Spectral analysis is done pixel by pixel for the non-thermal synchrotron emission with a realistic spectral index distribution and a fixed spectral index of $\beta = -2.1$ for the thermal bremsstrahlung emission.

Results. With the new method, we separate the non-thermal and thermal components of the Cygnus X region at an angular resolution of $9''.5$. The thermal emission component is found to comprise 75% of the total continuum emission at $\lambda 6$ cm. Thermal diffuse emission, rather than the discrete H II regions, is found to be the major contributor to the entire thermal budget. A smooth non-thermal emission background of 100 mK T_b is found. We successfully make the large-extent known supernova remnants and the H II regions embedded in the complex standing out, but no new large SNRs brighter than $\Sigma_{1\text{GHz}} = 3.7 \times 10^{-21} \text{ W m}^{-2} \text{ Hz}^{-1} \text{ sr}^{-1}$ are found.

Key words. Radio continuum: ISM – ISM: supernova remnants – H II regions

1. Introduction

The Galactic radio emission at decimetre and centimetre wavelengths is composited by the non-thermal synchrotron radiation generated by the relativistic electrons spiralling in the Galactic magnetic fields and the thermal bremsstrahlung (free-free) radiation originated from the interactions between electrons and ions. Separating the non-thermal and thermal emission components in the complex areas of the Galaxy helps to delineate the distribution of the electrons with different energy spectra, and identify new radio sources buried in the confusing environments.

To study the properties of interstellar medium and the foreground emission of the Cosmic Microwave Background, several methods have been developed to separate the Galactic emission into non-thermal synchrotron and thermal free-free emission. Hinshaw et al. (2007) used the maximum entropy method for the component separation for the WMAP data, where the extinction-corrected $H\alpha$ template (Finkbeiner 2003; Bennett et al. 2003) was used for the derivation of thermal free-free emission. Using the Effelsberg $\lambda 21$ cm (Reich et al. 1990b), $\lambda 11$ cm survey data (Reich et al. 1990a) together with the Parkes $\lambda 6$ cm data (Haynes et al. 1978), Paladini et al. (2005, here after P05) made the component separation for a thin layer of the inner Galactic plane ($20^\circ \leq \ell \leq 30^\circ$, $|b| \leq 1.5^\circ$) by fitting the observed Galactic emission by the thermal free-free emission with a fixed brightness temperature spectral index of $\beta = -2.1$ ($\alpha = \beta + 2$) and the non-thermal synchrotron emission with a $10''$ resolution spectral index distribution derived by Giardini et al. (2002). With a sim-

ilar method, Sun et al. (2011b) (hereafter S11) separated a much larger plane area of the inner Galaxy ($10^\circ \leq \ell \leq 60^\circ$, $|b| \leq 4^\circ$) by using the Effelsberg $\lambda 21$ cm (Reich et al. 1990b), $\lambda 11$ cm (Reich et al. 1990a), and the Urumqi $\lambda 6$ cm data, but with a fixed synchrotron spectral index. Using the radio recombination line as the tracer of thermal free-free emission, Alves et al. (2012) separated the non-thermal and thermal emission component for the region between $20^\circ \leq \ell \leq 40^\circ$ and $|b| \leq 4^\circ$. They claimed that the WMAP result greatly overestimates the thermal component in this area.

All these studies advanced our knowledge about the Galactic interstellar medium. However, WMAP has a coarse angular resolution of about 1° , which cannot be used for the studies of small-scale objects. The synchrotron spectral index distribution map used by P05 has an angular resolution of $10''$ and was derived by assuming that all the 408 MHz emission is purely non-thermal synchrotron emission. A fixed synchrotron spectral index assumed by S11 is too ideal for a practical situation.

With currently available data sets, we plan to develop a new method of component separation based on the work of P05. We aim to take a realistic synchrotron spectral index distribution with a higher angular resolution and study the properties of the non-thermal synchrotron and thermal free-free emission. The region we choose is the Cygnus X region, which is located at about $\ell \sim 80^\circ$ in the Galactic plane. It is one of the most famous and complex star forming sites in the Galaxy. It was first discovered and presented as a very extended bright source in the early radio observations (Piddington & Minnett 1952) and later resolved into many individual components by follow-up ob-

servations with higher angular resolutions and sensitivities (e.g. Wendker et al. 1991; Taylor et al. 1996; Landecker et al. 2010). Although many efforts have been made to study this big structure, the physical nature of the Cygnus X region remains unclear and is still under debate. The controversy lies on whether the Cygnus X region is a structure that the Local Arm is seen end-on (Wendker et al. 1991), or it is a huge coherent and physically bounded structure along the line of sight (e.g. Knödseder 2004; Schneider et al. 2006). Over two thousand massive stars are located in the Cygnus X region (Knödseder 2000). Therefore supernova explosions are expected and many SNRs should exist consequently. Observations made in the X-ray regime revealed a large bubble around the Cyg OB2 association, which might implies 30-100 supernovae explosions (Cash et al. 1980). However, up to date, only 12 SNRs have been found ($66^\circ \leq \ell \leq 90^\circ$, $|b| \leq 4^\circ$) according the Green SNR catalogue (Green 2009). It is thus interesting to search for new SNRs in the Cygnus X region. The very first step is to remove the strong confusion from the unrelated thermal emission.

In this paper, we develop a method for the non-thermal and thermal component separation, and search for new SNRs in the Cygnus X complex. We introduce the data sets we used in Sect. 2 and present the method and the test results in Sect. 3. We show our separation results of the Cygnus X region and make discussions in Sect. 4. A summary is given in Sect. 5.

2. Data

2.1. Data for construction of spectral index distribution of the Galactic emission and synchrotron emission

A proper separation of the thermal and non-thermal emission requires absolutely calibrated multi-frequency radio continuum data. Observations made at very high frequencies cannot be used, since the thermal dust and the anomalous microwave emission originated from the spinning dust will contribute to the observed radio emission; very low radio frequency observations also have to be skipped, because the thermal free-free emission will become optically thick and does not have the power law spectrum with the spectral index of $\beta \sim -2.1$. Therefore, data of the 408 MHz survey (Haslam et al. 1982), the Stockert 1420 MHz survey (Reich 1982), the Effelsberg 1408 MHz survey (Reich et al. 1990b) and the WMAP 22.8 GHz survey (Jarosik et al. 2011) are selected in our work to construct a realistic spectral index distribution for the observed Galactic emission and the synchrotron radiation at an angular resolution of 1° . The basic observational parameters of these surveys are listed in Table 1.

2.1.1. The 408 MHz survey

The 408 MHz all sky survey was combined by the survey data from the Jodrell Bank 76-m radio telescope, the Effelsberg 100-m radio telescope and the Parkes 64-m radio telescope (Haslam et al. 1982). The final released total intensity data has an angular resolution of $51'$ and was absolutely calibrated by the 404 MHz survey data (Pauliny-Toth & Shakeshaft 1962). The uncertainty of the 408 MHz total intensity data is better than 10%.

2.1.2. The Stockert 1420 MHz survey

The Stockert 1420 MHz survey covered the northern sky by using the 25-m Stockert radio telescope (Reich 1982). The angu-

lar resolution of the survey is 35.4 . The absolute calibration of the total intensity data was done by comparison with the horn observations (Howell & Shakeshaft 1966). The base level error and the uncertainty through the measurement of a single source are 0.5 K and 5%, respectively. By combining this survey with the 408 MHz survey, Reich & Reich (1988) derived the spectral index distribution of the observed Galactic emission of the northern sky, which is widely accepted and used.

2.1.3. The Effelsberg 1408 MHz survey

The Effelsberg 1408 MHz survey is a Galactic plane survey covering the range of $-3^\circ \leq \ell \leq 240^\circ$ in the Galactic longitude direction and $|b| \leq 4^\circ$ in the latitude direction (Reich et al. 1990b, 1997). The angular resolution of the survey is 9.4 . The Stockert 1420 MHz total intensity data was used to calibrate the 1408 MHz survey. The r.m.s. of the survey is about 40 mK T_b .

2.1.4. The WMAP K-band (22.8 GHz) survey

The K-band (22.8 GHz) WMAP data is at the lowest frequency among the five bands taken by the satellite. It contains negligible contributions of the thermal dust and the anomalous microwave emission. The angular resolution of the K-band data is 52.8 . The 7-year released data (Jarosik et al. 2011) is used in this study. The recently released 9-year data (Bennett et al. 2012) is discussed.

2.2. Data for high angular resolution component separation

To achieve a high angular resolution component separation, observations with better resolutions are needed. The Effelsberg 1408 MHz survey, the Effelsberg $\lambda 11$ cm and the Urumqi $\lambda 6$ cm survey have an angular resolution of 9.4 , 4.3 , and 9.5 , respectively, and therefore are used for this purpose. Note, however, that absolute calibration was not done for the Urumqi $\lambda 6$ cm total intensity data at all, and only partially done for the Effelsberg $\lambda 11$ cm survey in the Cygnus X region. The missing large-scale emission component must be restored in prior to the component separation (see details in Sect. 3).

2.2.1. The Urumqi $\lambda 6$ cm survey

The Urumqi $\lambda 6$ cm data of the Cygnus X region was extracted from a section of the Sino-German $\lambda 6$ cm polarization survey of the Galactic plane (Xiao et al. 2011)¹. The observations were conducted by the Urumqi 25-m radio telescope. The survey covers the Galactic plane from 10° to 230° in the Galactic longitude and $|b| \leq 5^\circ$ in the latitude, with an angular resolution of 9.5 . The uncertainty measured from a structureless area in the Cygnus X region was about 4 mK T_b .

2.2.2. The Effelsberg $\lambda 11$ cm survey

The Effelsberg $\lambda 11$ cm survey was conducted by the Effelsberg 100-m radio telescope (Fürst et al. 1990; Reich et al. 1990a). This survey has an angular resolution of 4.3 . The missing large-scale component was added by comparing with the Stockert $\lambda 11$ cm survey data (Reif et al. 1987), but only for the area of

¹ <http://zmtt.bao.ac.cn/6cm>

Table 1. Basic parameters of survey data in this work

Surveys	Frequency (MHz)	HPBW (')	Survey References	T_{off} (K)	References for T_{off}
$\lambda 73.5$ cm	408	51	Haslam et al. (1982)	2.7	Reich et al. (2004)
Stockert $\lambda 21$ cm	1420	35.4	Reich (1982)	2.8	Reich & Reich (1988)
Effelsberg $\lambda 21$ cm	1408	9.4	Reich et al. (1990b)	2.8	Reich et al. (1990b)
WMAP $\lambda 1.3$ cm	22800	52.8	Jarosik et al. (2011)	...	
Urumqi $\lambda 6$ cm	4800	9.5	Xiao et al. (2011)	...	
Effelsberg $\lambda 11$ cm	2700	4.3	Fürst et al. (1990); Reich et al. (1990a)	...	

Note: $T_{off} = T_{ex} + T_{cmb} + T_{zero}$, see Sect. 3 for detail.

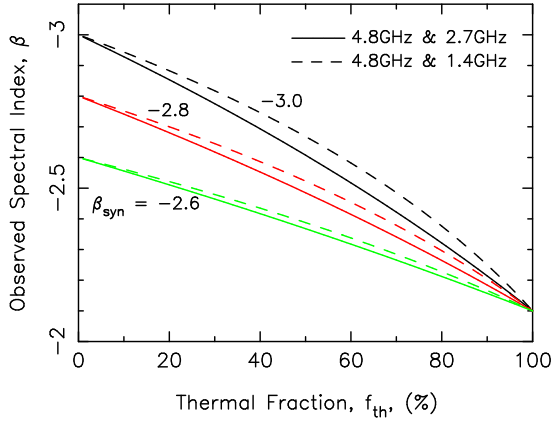


Fig. 1. Thermal fraction at $\lambda 6$ cm versus the spectral index β of observed Galactic emission. The spectral index of thermal free-free emission is fixed to be -2.1 , while the spectral index of non-thermal synchrotron emission is assumed to be -3.0 (black lines), -2.8 (red lines), and -2.6 (green lines), respectively. The curves calculated between $\lambda 6$ cm and $\lambda 11$ cm is shown by solid line and $\lambda 6$ cm and $\lambda 21$ cm by dashed line.

$-2^\circ \leq \ell \leq 76^\circ$, $|b| \leq 5^\circ$. The r.m.s of the survey data was about 25 mK T_b .

3. Method and test

3.1. Method

Our method for the component separation is based on the work of P05. The observed radio brightness temperature at frequency ν consists of several contributions (Reich & Reich 1988):

$$T_{obs}(\nu) = T_{gal}(\nu) + T_{cmb} + T_{ex}(\nu) + T_{zero}(\nu), \quad (1)$$

here, $T_{gal}(\nu)$ is the Galactic emission, composed by the thermal free-free and the non-thermal synchrotron emission, T_{cmb} is the 2.73 K contribution of the cosmic background, T_{ex} represents the component of the un-resolved extragalactic sources, and T_{zero} is the zero level of the data set to be corrected. The last three contributions comprise T_{off} ($T_{cmb} + T_{ex}(\nu) + T_{zero}(\nu)$), which should be subtracted first before the component separation. We got the values of T_{off} for each survey in literature and present them in Table 1.

After the T_{off} correction, we have the brightness temperature of the observed Galactic emission as being:

$$T_{gal}(\nu) = T_{th}(\nu) + T_{syn}(\nu), \quad (2)$$

here, $T_{th}(\nu)$ and $T_{syn}(\nu)$ are the thermal free-free and the non-thermal synchrotron radiation observed at a frequency ν . Both

of the two emission contributions have power law spectra but with different spectral indices. For observations at two different frequencies, we have:

$$T_{th}(\nu_1) = \left(\frac{\nu_1}{\nu_2}\right)^{\beta_{th}} T_{th}(\nu_2), \quad (3)$$

$$T_{syn}(\nu_1) = \left(\frac{\nu_1}{\nu_2}\right)^{\beta_{syn}} T_{syn}(\nu_2), \quad (4)$$

here β_{th} is the brightness temperature spectral index of the thermal free-free emission, while β_{syn} is that for the non-thermal synchrotron emission. As noted by P05, two power laws added together does not make another power law. However, we can always find a directly derived spectral index “ β ” for the observed brightness temperatures at two bands (see Equation 5). We show the changes of β for wavelength pairs as a function of thermal emission fraction in Fig. 1. We emphasize here that β varies with different frequency pairs and with thermal (non-thermal) fractions.

$$T_{gal}(\nu_1) = \left(\frac{\nu_1}{\nu_2}\right)^{\beta} T_{gal}(\nu_2), \quad (5)$$

Combining the Eq. 3 to 5, as done by P05, we easily derived the thermal fraction at frequency ν_1 as:

$$f_{th\nu_1} = \frac{1 - \left(\frac{\nu_2}{\nu_1}\right)^{\beta - \beta_{syn}}}{1 - \left(\frac{\nu_2}{\nu_1}\right)^{\beta_{th} - \beta_{syn}}}, \quad (6)$$

This equation is the key to all of the following derivations. We explain our algorithm for the component separation in below. We first subtracted T_{off} in the 408 MHz, Stockert 1420 MHz, Effelsberg 1408 MHz maps and the dust template² from the WMAP K-band map. Then they are convolved to a common angular resolution of 1° . According to Eq. 6, the 408 MHz and the Stockert 1420 MHz data can be used to calculate the thermal fraction at 1420 MHz, while the Effelsberg 1408 MHz and the WMAP 22800 MHz data can be used for the derivation of the thermal fraction at 1408 MHz. The two fraction values should be the same at nearly the same frequency. The spectral index of observed Galactic emission were calculated pixel by pixel as $\beta_{408-1420} = \frac{\log(T_{408}/T_{1420})}{\log(408/1420)}$ and $\beta_{1408-22800} = \frac{\log(T_{1408}/T_{22800})}{\log(1408/22800)}$ according to the Eq. 5. The thermal brightness temperature spectral index is set to a fixed value of $\beta_{ff} = -2.1$. The only unknown non-thermal synchrotron emission spectral index β_{syn} in Eq. 6 is being fitted in the range of -2.1 to -3.0 . If the thermal fractions ($f_{th1.4GHz}$) calculated from the 408/1420 data pair and the 1408/22800 data pair have a difference less than 5%, the β_{syn} is recorded. Such a group of β_{syn} is finally averaged and taken as

² http://lambda.gsfc.nasa.gov/product/map/dr4/mem_maps_get.cfm

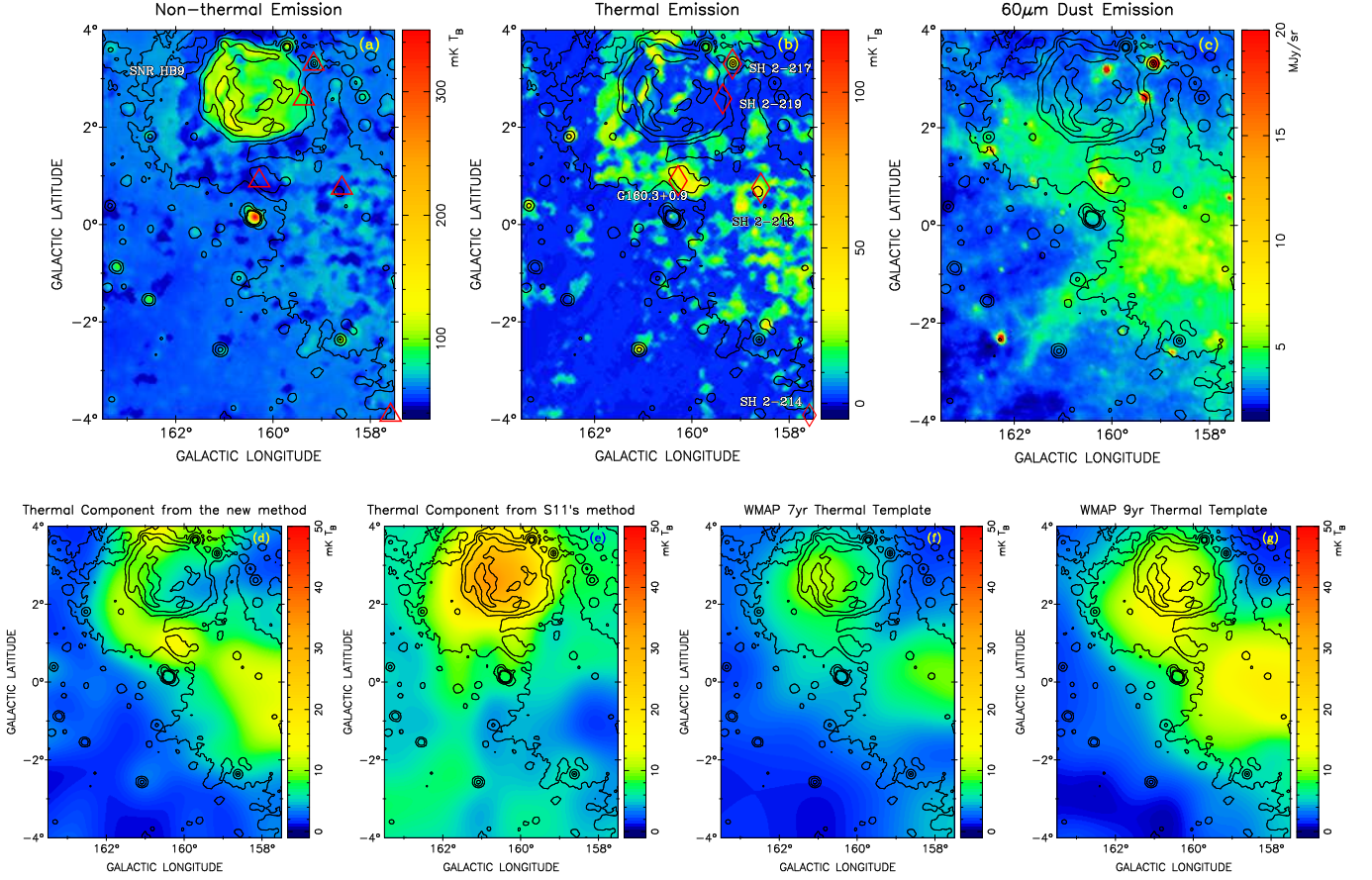


Fig. 2. Maps for the test region. *Upper panels:* high-resolution (9'5) images of decomposed non-thermal (*panel a*) and thermal (*panel b*) emission at $\lambda 6$ cm overlaid by contours of the $\lambda 6$ cm total intensity (not decomposed). The contour lines run in 50, 65, 80, 105 and 120 mK T_b . The SNR HB9 is labelled with name, while the known H II regions are labelled with diamonds and names. *panel c:* the IRIS 60 μ m image overlaid by the same contours as in *panel a* and *b*. Images in the *lower panels* are convolved to an angular resolution of 1°, and overlaid by the same contours as in the *upper panels*. Decomposed thermal emission component by using our method (*panel d*) is compared with that by Sun et al. (2011b)'s method (*panel e*) and WMAP 7-year and 9-year free-free templates (*panel f* and *g*).

the final solution for the pixel. If no β_{syn} fits for a pixel, we set the thermal fraction $f_{th,1.4GHz}$ as the average value of the surrounding pixels and then calculate β_{syn} . If both $\beta_{408-1420}$ and $\beta_{1408-22800}$ are larger than -2.1 , the emission is overwhelmingly contributed by the thermal emission. The non-thermal emission of the pixel is taken as that from the nearest pixels where the calculation is possible. After this procedure, we got the map of thermal fraction, and the brightness temperature map of thermal emission at 1.4 GHz at an angular resolution of 1°. Non-thermal emission map is then calculated by subtracting the thermal emission map from the 1408 MHz total intensity map. With the spectral index $\beta_{th} = -2.1$ and the β_{syn} pixel by pixel, the thermal and non-thermal emission components can be separated from observations at any frequencies.

The separated components obtained above have an angular resolution of 1°. By taking the data from the Urumqi $\lambda 6$ cm, Effelsberg $\lambda 11$ cm and the Effelsberg $\lambda 21$ cm (1408 MHz) survey, a decomposition at an angular resolution 9'5 can be made. However, as described in Sect. 2, both of the $\lambda 6$ cm and $\lambda 11$ cm total intensity data miss the large-scale emission component. T_{zero} must be corrected in prior to the separation. S11 developed a method for the base-level restoration for the Urumqi survey towards the inner Galactic plane area. Their method requires structureless edges of the map in the latitude direction. It is not appli-

cable to the Cygnus X region, since the complex is too extended, exceeding 4° in b . We therefore restored the missing large-scale component for the $\lambda 6$ cm data according to the method introduced by Reich et al. (1990b). We first extrapolated the 1° angular resolution Effelsberg 1408 MHz thermal and non-thermal emission component to $\lambda 6$ cm by using β_{th} and β_{syn} , pixel by pixel. The sum of the two extrapolated components was set as a fully calibrated template which contains the emission from all scales. Then we convolved the originally observed $\lambda 6$ cm data to the same angular resolution of 1° and compare with the template. The difference is calculated and added back to the observed $\lambda 6$ cm data as the missing large-scale component. The same procedure is done for the Effelsberg $\lambda 11$ cm data. Then the Effelsberg $\lambda 11$ cm and $\lambda 21$ cm data were convolved to the angular resolution of 9'5, the same as the Urumqi $\lambda 6$ cm data. Following the algorithm we introduced above, component separation with a higher angular resolution can be realized at the wavelength of $\lambda 6$ cm.

3.2. Results for a test region

In order to verify the capability of our new method, a region of $158.5^\circ \leq \ell \leq 163.5^\circ$, $|b| \leq 4^\circ$, involving the well-known SNR HB9, some H II regions and diffuse emission was firstly

tested qualitatively. We showed the decomposition results in the *upper panel* of the Fig. 2. The maps show reasonable results for many sources. The SNR HB9 and many extra-Galactic sources e.g. four extra-Galactic sources located around $\ell \sim 158^\circ.5, b \sim 2^\circ.7$ in the west of HB9, the sources at $\ell = 163^\circ.35, b = 0^\circ.35, \ell = 163^\circ.20, b = -0^\circ.90, \ell = 162^\circ.55, b = -1^\circ.55$, and $\ell = 160^\circ.70, b = -1^\circ.15$ clearly show up in the separated non-thermal component image (Fig. 2, *panel a*) as expected. Free-free emission of the large H II region SH 2-216 ($1^\circ.6$ in diameter Tweedy et al. 1995), and the H II region G160.3+0.9 (Blitz et al. 1982; Kuchar & Clark 1997) are successfully separated into the thermal component map (Fig. 2, *panel b*). Thermal emission associated with the H II region SH 2-214 ($\ell = 157^\circ.60, b = -3^\circ.91$) is not seen, since no clear radio counterpart of this object was detected at $\lambda 6$ cm.

We further cross check the output of the new method with that from S11's method, and those from the free-free emission template of the 7-year (Gold et al. 2011) and 9-year WMAP data (Bennett et al. 2012) extrapolated from $\lambda 1.3$ cm to $\lambda 6$ cm with the brightness temperature spectral index of $\beta = -2.1$, at the same angular resolution of 1° . It is important and necessary to do these comparisons, since our method and that of S11 both rely on the radio continuum data and the determination of the non-thermal spectral indices, while the WMAP template is independent, using the H α data to estimate the contribution from the thermal free-free emission. The comparison is shown in the lower panels of the Fig. 2 and we found our result is better. Generally, the thermal emission component map produced by our new method show similar structures as shown in the WMAP templates. However, the images from the WMAP templates and the S11 method unexpectedly show a large amount of thermal emission within the SNR HB9, which is supposed to be a purely non-thermal source. S11 explained this leakage as a result from a fixed non-thermal synchrotron spectral index. For the large thermal H II region SH 2-216, we found structural resemblance between radio emission and the IRIS $60\mu\text{m}$ infrared dust emission (Miville-Deschênes & Lagache 2005), which confirms the thermal property of the large area. The thermal emission of SH 2-216 is well separated out by our method, and also shown in the two WMAP templates, but very little thermal emission can be separated out by S11's method. We noticed that the thermal emission of SH 2-216 figured out by our method is less than that in the WMAP 9-year template, but more than that in the WMAP 7-year template. We do not understand the big difference between the two templates.

Another indication of validation of the new method comes from an identical structure to the southeast of the SNR HB9. Radio emission in this region can be well separated in the thermal component map and seen in the images shown in Fig. 2 by all of the four methods. Strong infrared emission in this region is detected in the IRIS $60\mu\text{m}$ image, implying its thermal nature.

"Leakage", however, is still seen in a few sources, perhaps due to the fluctuations in the data pixels from the observations. For example, the thermal H II region SH 2-217 ($\ell = 159^\circ.16, b = 3^\circ.30$) is partially seen in the non-thermal emission image.

4. Application of the new method to the Cygnus X region

After proving the applicability of the new method, we apply it to decompose the thermal and non-thermal emission components in the Cygnus X region. As noticed above that the WMAP 7-year and 9-year data show discrepancies in the test region. We

involved the two versions of the WMAP data in our calculation alternatively. The 7-year data gives more reasonable result and is finally used. We show in Fig. 3 the spectral index β maps of the observed Galactic emission in the Cygnus X region derived between the Urumqi $\lambda 6$ cm and Effelsberg $\lambda 21$ cm (1408 MHz) data, and between the Urumqi $\lambda 6$ cm and Effelsberg $\lambda 11$ cm data, and present in Fig. 4 the separation result of the thermal and non-thermal components. The spectral index map derived between $\lambda 6$ cm and $\lambda 21$ cm is much smoother than that from $\lambda 6$ cm and $\lambda 11$ cm. We suspect that it is partially due to the small frequency separation and partially due to scanning effect in the $\lambda 11$ cm survey, shown as horizontal stripes around $\ell \sim 81^\circ$ in the separation results as shown in Fig. 3. The first glance of the overall structure decomposed by the new method confirms the conclusions of Wendker et al. (1991) that nearly all the prominent radio radiation from the Cygnus X region comes from the thermal free-free emission. Many elongated thermal ridges are identical to what they have discovered. All known H II regions listed by Sharpless (1959) and Paladini et al. (2003) are found to have thermal emission in the separated image, which can be verified by the IRIS $60\mu\text{m}$ image (see Fig. 4, *panel d*).

4.1. Diffuse emission

Non-thermal radiation in the Cygnus X region is weak and diffuse (see Fig. 4, *panel b*). No significant enhancement in synchrotron radiation across the longitude range of 66° to 90° is noticed. This does not conflict with the point of view that the Cygnus X region is a complex that the local arm is seen end-on (Wendker et al. 1991). Either because the local arm has a certain width and our angle of view might not exceed this scale and/or the local arm is relatively fainter than the major arms, that the non-thermal radiation we see in this region is predominately contributed by the farther Perseus arm. The r.m.s of the non-thermal component image is about 20 mK T_b at $\lambda 6$ cm. Although the image appears to be mottled, which we believe was introduced by the uncertainties in the data, the intensity in large scales is uniform in general, around 100 mK T_b at $\lambda 6$ cm. This quantity, shown as the gap between the total power and thermal emission profiles in Fig. 5 is always standing there even by the three different methods. With the non-thermal emission components separated at $\lambda 21$ cm, $\lambda 11$ cm and $\lambda 6$ cm, discarding the regions of the known SNRs, we estimate the average synchrotron spectral index of the Cygnus X region as being $\beta_{\text{syn}} = -2.8 \pm 0.1$.

The distribution of thermal radiation concentrates in two areas (see Fig. 4, *panel c*). One is the main part of the Cygnus X region, in the centre of the map, about 9° span in the Galactic longitude direction. The majority of known H II regions can be found in this region. The other area with enhanced thermal emission is W80 ($\ell \sim 85^\circ, b \sim -0^\circ.9$), whose optical counterpart contains the well-known North America and the Pelican Nebulae. The thermal radiation in both of the areas account for $\sim 75\%$ of the total intensity of the $\lambda 6$ cm continuum emission.

For the large-scale thermal emission, we statistically compared the one-dimensional averaged results derived by our method, S11's method and the WMAP template at $\lambda 6$ cm at an angular resolution of 1° . The intensity of each pixel is averaged in the longitude direction and the profiles are shown in Fig. 5. The three profiles highly resemble each other and the decomposition failures in the individual sources (like the case of SNR HB9) do not affect the statistics on very large scales, as noted by S11.

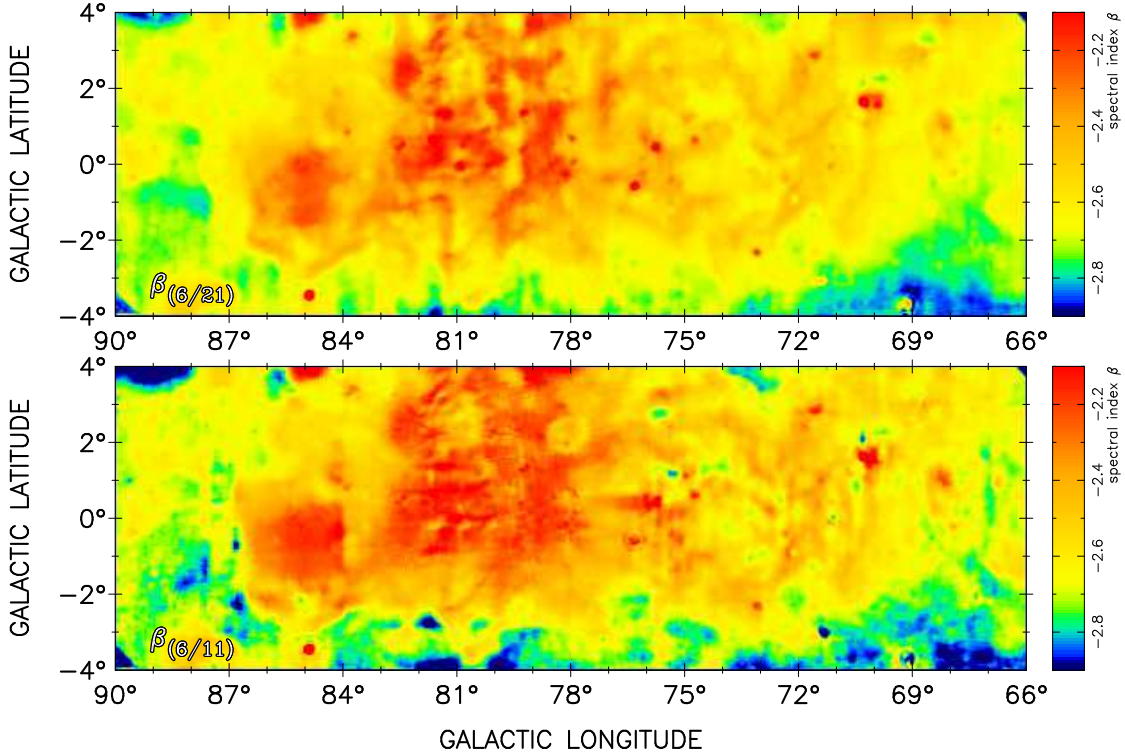


Fig. 3. Spectral index maps of the Galactic emission derived from survey maps at $\lambda 6$ cm and $\lambda 21$ cm bands (*upper panel*) and at $\lambda 6$ cm and $\lambda 11$ cm bands (*lower panel*).

4.2. Uncertainty of results

A qualitative comparison in Fig. 2 shows that the new separation method performs better in details than the other methods. In a statistical sense, the new method gives consistent results with that by the WMAP template and the S11's method (see Fig. 5). Here we estimate of the uncertainties of the separation result of the Cygnus X region. From the errors of the low resolution surveys, an uncertainty of 5% was estimated for the $\lambda 6$ cm and $\lambda 11$ cm data after the restoration of the missing large-scale emission. Based on the standard error propagation, the uncertainty of the separated thermal and non-thermal components derived by the new method with the Effelsberg $\lambda 21$ cm, $\lambda 11$ cm and the Urumqi $\lambda 6$ cm data as we showed in the Fig. 4 is about 17%. As noted by Wendker et al. (1991), the accuracy in the low emission area, usually the data points away from the Galactic plane near edges of the image, tends to be worse than that for the area of strong emission with high S/N ratios. We tested the pixels near the boundary of the separated map, and found the uncertainties are indeed higher, but at most 30%.

4.3. Notes on discrete sources

According to Paladini et al. (2003), 145 individually known H II regions are located in the Cygnus X region. We summed their flux density according to the Paladini catalogue and extrapolate it to $\lambda 6$ cm band by the spectral index of $\beta = -2.1$. We found that the individual H II regions only account for 4% of the total thermal emission at $\lambda 6$ cm. This might be the lower limit, since H II regions are difficult to identify in such a complex area. However, undoubtedly, diffuse thermal emission overwhelmingly dominates the whole thermal emission budget.

There are 12 known supernova remnants in the catalog of Green (2009) in the region ranging of $66^\circ \leq \ell \leq 90^\circ$, $|b| \leq 4^\circ$.

Two large SNRs, G78.2+2.1 (DR4) and G69.0+2.7 (CTB 80) have already been studied in Gao et al. (2011) with the Urumqi $\lambda 6$ cm survey data, while five small SNRs, i.e. G73.9+0.9, G74.9+1.2, G76.9+1.0, G84.2-0.8 and G85.9-0.6 were investigated in Sun et al. (2011a). From the non-thermal emission component shown in Fig. 4, both SNR G78.2+2.1 and CTB 80 are clearly separated out by the new method. In the original map, the SNR G78.2+2.1 is heavily confused by the strong thermal emission and the surrounding structures. Gao et al. (2011) used the “background filtering” technique (Sofue & Reich 1979) and subtracted a fitted twisted hyper plane to eliminate the un-related non-thermal background and the ambient thermal emission (see Fig. 1 of Gao et al. 2011). The image of Fig. 4 (b) from the new method show less contamination of thermal emission by successfully getting rid of the confusion from the H II region G78.3+2.8 in the north, IC 1318b in the south and southeast, and perhaps also the contribution of the un-related small H II region, γ Cygni nebula, which coincides in the southern shell of the SNR G78.2+2.1. The $\lambda 6$ cm integrated flux density for this SNR is now found to be ~ 140 Jy, consistent with the result found by Gao et al. (2011). Faint non-thermal radiation is seen in the south, north-west and north-east of the SNR G78.2+2.1. We suppose that these might result from “leakages”.

Besides the two large SNRs, we can see the SNRs G73.9+0.9, G74.9+1.2, G84.2-0.8 and G85.9-0.6 from the separated map. The later two are much fainter than their measured intensity (Sun et al. 2011a). This is not the “leakage” problem but due to the data we used. The spectral indices β of the two SNRs derived between $\lambda 6$ cm and $\lambda 11$ cm are both around ~ -2.2 , too flat for shell-type SNRs. We cannot separate out the SNR G76.9+1.0, since no solution can be matched between the data pair of 1408 MHz/4800 MHz and 2700 MHz/4800 MHz. The remaining five SNRs G67.7+1.8, G68.6-1.2, G69.7+1.0, G85.4+0.7 and G83.0-0.3 were not included in any previous

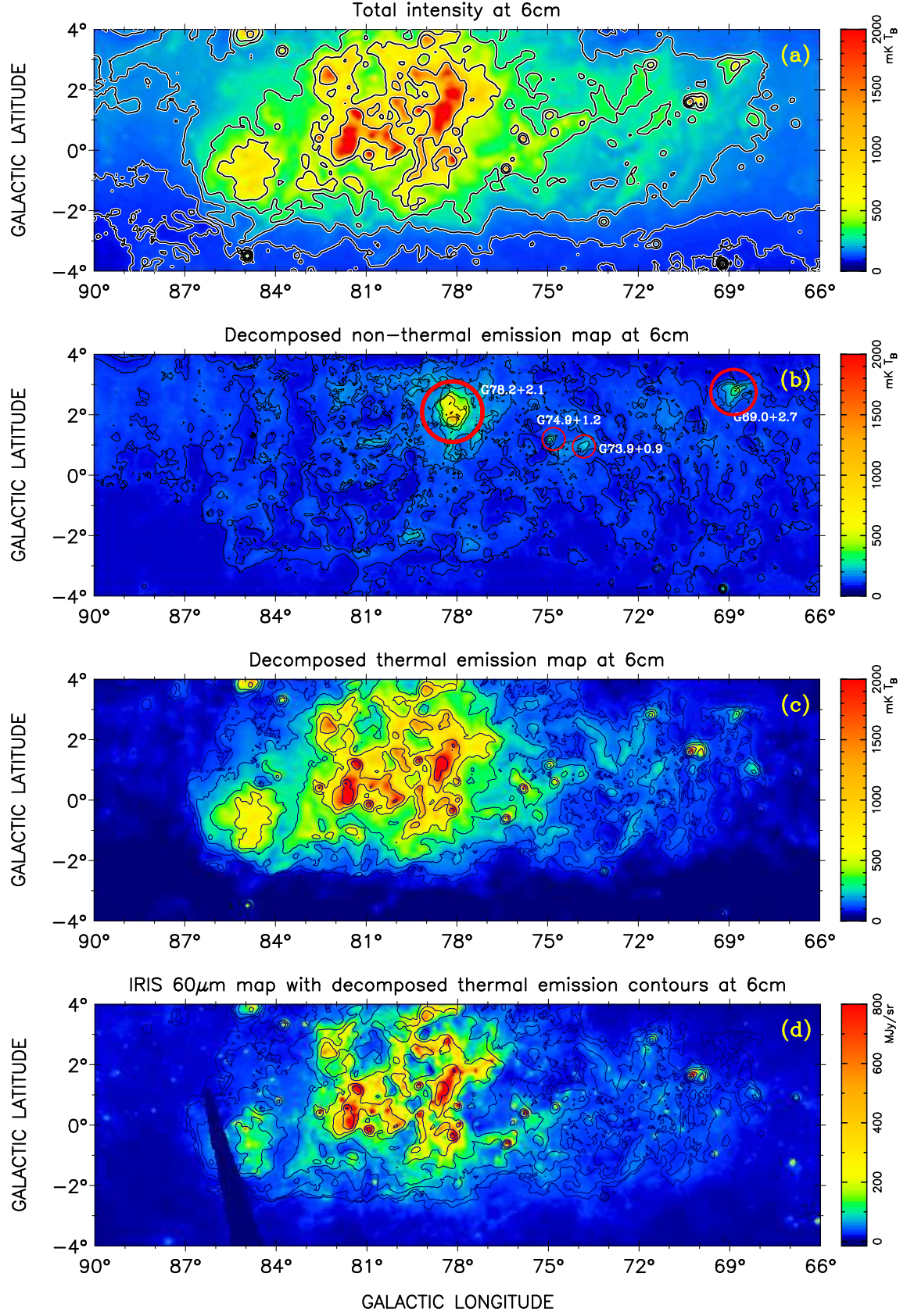


Fig. 4. The $\lambda 6$ cm radio maps of total intensity (*panel a*), decomposed non-thermal (*panel b*) and thermal (*panel c*) emission in the Cygnus X region at an angular resolution of $9''.5$. The IRIS 60 μ m image (*panel d*) of the Cygnus X region is shown for comparison with the decomposed thermal map. Contours in *panel a* and *c* are running in steps of $70 + 2^{n-1} \times 30$ mK T_b ($n = 0, 1, 2, \dots$). The contours in *panel b* for non-thermal emission run in 100, 150, 200, 300, 500 and 800 mK T_b . Contours in *panel d* are the same as those in *panel c*. The visible SNRs are indicated in *panel b*.

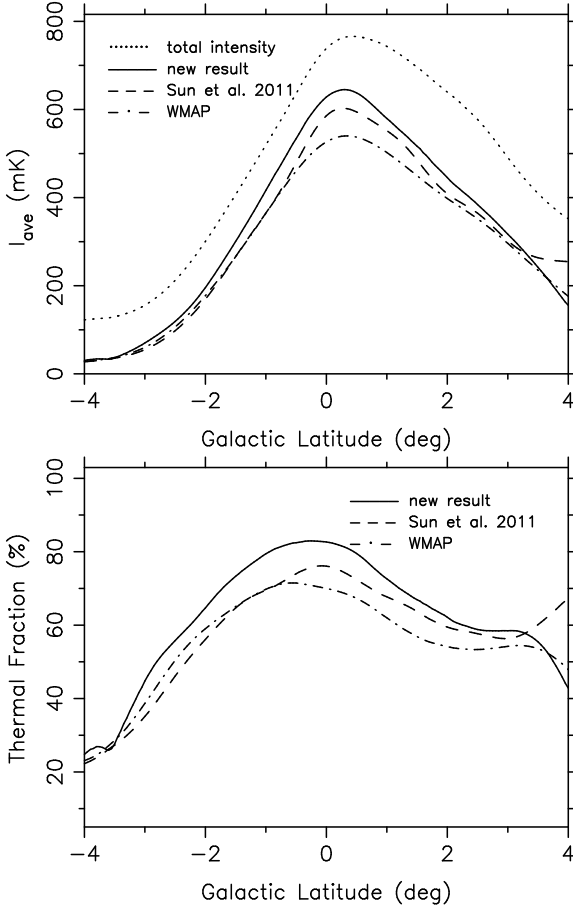


Fig. 5. Galactic latitude profiles for the averaged intensities (*upper panel*) and averaged thermal fractions (*lower panel*) at 16 cm in the Cygnus X region ($77^\circ \leq \ell \leq 87^\circ$, $|b| \leq 4^\circ$). The dotted line is the 16 cm total intensity. The thermal component derived from our method, S11’s method and WMAP template are presented by solid line, dashed line and dash-dot line, respectively.

Urumqi 16 cm studies. All of them are faint and less than 30’ in diameter, structureless as seen with our 9.5’ beam. The first three were deeply embedded in the radio complex of W80. We do see some signatures of these objects in the decomposed non-thermal emission image, however, they are fragmented. “Leakages” to the thermal emission with various amounts are detected for all of them, thus no good measurement can be made.

Apart from the known SNRs, we carefully checked the spectral index distributions of observed Galactic and the suspicious structures in the non-thermal emission image for possible new SNRs, but failed to find any new features. We estimate the surface brightness limit of the decomposed non-thermal emission map by using the equation $\Sigma_{1\text{GHz}} = 1.505 \times 10^{-19} S_{6\text{cm}} / \theta^2$, here $S_{1\text{GHz}}$ is obtained by extrapolating $S_{6\text{cm}} = 1 \text{ Jy}$ (160 mK), the 3σ level above the non-thermal background emission (100 mK) to 1 GHz, using the typical spectral index of $\alpha = -0.5$ for shell-type SNRs, θ is the beam size of 9.5, the smallest scale of sources that can be seen in the data. We finally conclude that no new large-extent SNRs brighter than $\Sigma_{1\text{GHz}} = 3.7 \times 10^{-21} \text{ W m}^{-2} \text{ Hz}^{-1} \text{ sr}^{-1}$ can be found in our separated non-thermal image of the Cygnus X region.

5. Summary

We developed a new method which can be used to separate the thermal free-free and the non-thermal synchrotron emission components by using the centimetre radio continuum survey data. The new method is applied to the Cygnus X complex region. We found that the thermal free-free emission comprises 75% of the total continuum radiation in the Cygnus X region at 16 cm. We compared the large-scale thermal structures decomposed by the new method with that derived from the WMAP data, and found that they are consistent with each other. An uniform non-thermal background in the Cygnus X region is found to be $100 \pm 20 \text{ mK}$ at 16 cm. The separation by using the Effelsberg 121 cm, 111 cm and the Urumqi 16 cm maps enables us to search for new large and faint SNRs in the Cygnus X region at an angular resolution of 9.5. However, no new large-extent SNRs brighter than $\Sigma_{1\text{GHz}} = 3.7 \times 10^{-21} \text{ W m}^{-2} \text{ Hz}^{-1} \text{ sr}^{-1}$ are discovered.

Acknowledgements. The authors would like to thank the anonymous referee for constructive suggestions, and Dr. Wolfgang Reich and Dr. Xiaohui Sun for helpful discussions. XWF would like to thank Mr. Tao Hong in helping with the production of plots and carefully reading the manuscript. The authors are supported by the National Natural Science foundation of China (10773016, 11303035 and 11261140641) and XYG is additionally supported by the Young Researcher Grant of National Astronomical Observatories, Chinese Academy of Sciences.

References

- Alves, M. I. R., Davies, R. D., Dickinson, C., et al. 2012, MNRAS, 422, 2429
- Bennett, C. L., Halpern, M., Hinshaw, G., et al. 2003, ApJS, 148, 1
- Bennett, C. L., Larson, D., Weiland, J. L., et al. 2012, ApJS, accepted [arXiv:1212.5225]
- Blitz, L., Fich, M., & Stark, A. A. 1982, ApJS, 49, 183
- Cash, W., Charles, P., Bowyer, S., et al. 1980, ApJ, 238, L71
- Finkbeiner, D. P. 2003, ApJS, 146, 407
- Fürst, E., Reich, W., Reich, P., & Reif, K. 1990, A&AS, 85, 691
- Gao, X. Y., Han, J. L., Reich, W., et al. 2011, A&A, 529, A159
- Giardino, G., Banday, A. J., Górski, K. M., et al. 2002, A&A, 387, 82
- Gold, B., Odegard, N., Weiland, J. L., et al. 2011, ApJS, 192, 15
- Green, D. A. 2009, Bull. Astron. Soc. India, 37, 45
- Haslam, C. G. T., Salter, C. J., Stoffel, H., & Wilson, W. E. 1982, A&AS, 47, 1
- Haynes, R. F., Caswell, J. L., & Simons, L. W. J. 1978, Australian Journal of Physics Astrophysical Supplement, 45, 1
- Hinshaw, G., Nolte, M. R., Bennett, C. L., et al. 2007, ApJS, 170, 288
- Howell, T. F., & Shakeshaft, J. R. 1966, Nature, 210, 1318
- Jarosik, N., Bennett, C. L., Dunkley, J., et al. 2011, ApJS, 192, 14
- Knödlseider, J. 2000, A&A, 360, 539
- Knödlseider, J. 2004 [arXiv:astro-ph/0407050]
- Kuchar, T. A., & Clark, F. O. 1997, ApJ, 488, 224
- Landecker, T. L., Reich, W., Reid, R. I., et al. 2010, A&A, 520, A80
- Miville-Deschênes, M., & Lagache, G. 2005, ApJS, 157, 302
- Paladini, R., Burigana, C., Davies, R. D., et al. 2003, A&A, 397, 213
- Paladini, R., De Zotti, G., Davies, R. D., & Giard, M. 2005, MNRAS, 360, 1545 (P05)
- Pauliny-Toth, I. K., & Shakeshaft, J. R. 1962, MNRAS, 124, 61
- Piddington, J. H., & Minnett, H. C. 1952, Australian Journal of Scientific Research A Physical Sciences, 5, 17
- Reich, P., & Reich, W. 1988, A&AS, 74, 7
- Reich, P., Reich, W., & Fürst, E. 1997, A&AS, 126, 413
- Reich, P., Reich, W., & Testori, J. C. 2004, in The Magnetized Interstellar Medium, ed. B. Uyaniker, W. Reich, & R. Wielebinski, 63–68
- Reich, W. 1982, A&AS, 48, 219
- Reich, W., Fürst, E., Reich, P., & Reif, K. 1990a, A&AS, 85, 633
- Reich, W., Reich, P., & Fürst, E. 1990b, A&AS, 83, 539
- Reif, K., Reich, W., Steffen, P., Müller, P., & Weiland, H. 1987, Mitteilungen der Astronomischen Gesellschaft Hamburg, 70, 419
- Schneider, N., Bontemps, S., Simon, R., et al. 2006, A&A, 458, 855
- Sharpless, S. 1959, ApJS, 4, 257
- Sofue, Y., & Reich, W. 1979, A&AS, 38, 251
- Sun, X. H., Reich, P., Reich, W., et al. 2011a, A&A, 536, A83
- Sun, X. H., Reich, W., Han, J. L., et al. 2011b, A&A, 527, A74 (S11)
- Taylor, A. R., Goss, W. M., Coleman, P. H., van Leeuwen, J., & Wallace, B. J. 1996, ApJS, 107, 239

- Tweedy, R. W., Martos, M. A., & Noriega-Crespo, A. 1995, *ApJ*, 447, 257
Wendker, H. J., Higgs, L. A., & Landecker, T. L. 1991, *A&A*, 241, 551
Xiao, L., Han, J. L., Reich, W., et al. 2011, *A&A*, 529, A15